



HAL
open science

Globally coherent water cycle response to temperature changes during the past two millennia

Bronwen Konecky, Guillaume Leduc, Marie-Alexandrine Sicre, Emilie Pauline Dassié

► **To cite this version:**

Bronwen Konecky, Guillaume Leduc, Marie-Alexandrine Sicre, Emilie Pauline Dassié. Globally coherent water cycle response to temperature changes during the past two millennia. *Nature Geoscience*, 2023. hal-04301540

HAL Id: hal-04301540

<https://hal.science/hal-04301540>

Submitted on 23 Nov 2023

HAL is a multi-disciplinary open access archive for the deposit and dissemination of scientific research documents, whether they are published or not. The documents may come from teaching and research institutions in France or abroad, or from public or private research centers.

L'archive ouverte pluridisciplinaire **HAL**, est destinée au dépôt et à la diffusion de documents scientifiques de niveau recherche, publiés ou non, émanant des établissements d'enseignement et de recherche français ou étrangers, des laboratoires publics ou privés.



Distributed under a Creative Commons Attribution 4.0 International License

1 **Title: Globally coherent water cycle response to temperature changes during**
2 **the past two millennia**
3

4 **Authors:** Bronwen L. Konecky^{1*}, Nicholas P. McKay², Georgina M. Falster^{1,3}, Samantha L. Stevenson⁴, Matt J.
5 Fischer⁵, Alyssa R. Atwood⁶, Diane M. Thompson⁷, Matthew D. Jones⁸, Jonathan J. Tyler⁹, Kristine L. DeLong¹⁰,
6 Belen Martrat¹¹, Elizabeth K. Thomas¹², Jessica L. Conroy¹³, Sylvia G. Dee¹⁴, Lukas Jonkers¹⁵, Olga V. Churakova
7 (Sidorova)^{16,17}, Zoltán Kern^{18,19}, Thomas Opel²⁰, Trevor J. Porter²¹, Hussein R. Sayani²², Grzegorz Skrzypek²³, and
8 Iso2k Project Members[†]
9

10 **Affiliations:**

11 ¹Department of Earth and Planetary Sciences, Washington University, Saint Louis, Missouri, 63108, USA

12 ²School of Earth and Sustainability, Northern Arizona University, Flagstaff, AZ, 86011, USA

13 ³Research School of Earth Sciences and ARC Centre of Excellence for Climate Extremes, Australian National
14 University, Canberra, ACT, 2601, Australia

15 ⁴Bren School of Environmental Science & Management, University of California, Santa Barbara, Santa
16 Barbara, CA, 93106, USA

17 ⁵NSTLI Environment, ANSTO, Sydney, NSW, 2234, Australia

18 ⁶Department of Earth, Ocean, and Atmospheric Sciences, Florida State University, Tallahassee, Florida, 32306,
19 USA

20 ⁷Department of Geosciences, University of Arizona, Tucson, Arizona, 85719, USA

21 ⁸School of Geography, University of Nottingham, Nottingham, NG7 2RD, UK

22 ⁹Department of Earth Sciences, The University of Adelaide, Adelaide, South Australia, 5005, Australia

23 ¹⁰Department of Geography and Anthropology, Coastal Studies Institute, Louisiana State University, Baton
24 Rouge, LA, 70803, USA

25 ¹¹Department of Environmental Chemistry, Institute of Environmental Assessment and Water Research
26 (IDAEA-CSIC), Barcelona, Barcelona, 08034, Spain

27 ¹²Department of Geology, University at Buffalo, Buffalo, NY, 14260, USA

28 ¹³Department of Geology, Department of Plant Biology, University of Illinois at Urbana-Champaign, Urbana,
29 IL, 61822, USA

30 ¹⁴Department of Earth, Environmental, and Planetary Sciences,, Rice University, Houston, Texas, 77005, USA

31 ¹⁵MARUM Center for Marine Environmental Sciences, Bremen University, Bremen, 28359, Germany

32 ¹⁶Institute of Ecology and Geography, Siberian Federal University, Krasnoyarsk, 660041, Russian Federation

33 ¹⁷Department of Forest Dynamics, Swiss Federal Institute for Forest, Snow and Landscape Research WSL,
34 Birmensdorf, CH-8903, Switzerland

35 ¹⁸Institute for Geological and Geochemical Research, Research Centre for Astronomy and Earth Sciences,
36 Eötvös Loránd Research Network, Budapest, H-1112, Hungary

37 ¹⁹CSFK, MTA Centre of Excellence, Budapest, H-1121, Hungary

38 ²⁰Polar Terrestrial Environmental Systems, Alfred Wegener Institute Helmholtz Centre for Polar and Marine
39 Research, Potsdam, 14473, Germany

40 ²¹Department of Geography, Geomatics and Environment, University of Toronto - Mississauga, Mississauga,
41 Ontario, L5L1C6, Canada

42 ²²School of Earth and Atmospheric Science, Georgia Institute of Technology, Atlanta, GA, 30332, USA

43 ²³West Australian Biogeochemistry Centre, School of Biological Sciences, The University of Western Australia,
44 Perth, Western Australia, 6009, Australia
45
46
47

48 † Iso2k Project Members includes all above named authors and: Nerilie J. Abram (Australian National
49 University, Australia), Kerstin Braun (Arizona State University, USA), Matthieu Carré (Sorbonne Universités
50 (UPMC)-CNRS-IRD-MNHN, France), Olivier Cartapanis (Aix-Marseille University, France), Laia Comas-Bru
51 (University of Reading, United Kingdom), Mark A. Curran (Australian Antarctic Division, Australia), Emilie P.
52 Dassié (University of Bordeaux, France), Michael Deininger (Johannes Gutenberg University Mainz,
53 Germany), Dmitry V. Divine (Norwegian Polar Institute, Norway), Alessandro Incarbona (Palermo University,
54 Italy), Darrell S. Kaufman (Northern Arizona University, USA), Nikita Kaushal (University of Oxford, United
55 Kingdom), Robert M. Klabe (The University of Adelaide, Australia), Hannah R. Kolus (Northern Arizona
56 University, USA), Guillaume Leduc (Aix Marseille University, CNRS, IRD, INRAE, Coll France, CEREGE,
57 France), Shreyas R. Managave (Indian Institute of Science Education and Research, India), P. Graham Mortyn
58 (Universitat Autònoma de Barcelona (UAB), Spain), Andrew D. Moy (Australian Antarctic Division,
59 Australia), Anais J. Orsi (Laboratoire des Sciences du Climat et de L'Environnement, France), Judson W. Partin
60 (University of Texas at Austin, USA), Heidi A. Roop (University of Minnesota, USA), Marie-Alexandrine
61 Sicre (CNRS and Sorbonne Université, France), Lucien von Gunten (PAGES International Project Office,
62 Switzerland), and Kei Yoshimura (The University of Tokyo, Japan)

63
64

65 * Corresponding author. Email: bkonecky@wustl.edu

66
67

68

69

70

71

72

73

74

75

76 **The response of the global water cycle to changes in global surface temperature remains an**
77 **outstanding question in future climate projections and past climate reconstructions. The**
78 **stable hydrogen and oxygen isotope compositions of precipitation (δ_{precip}), meteoric water**
79 **(δ_{MW}), and seawater (δ_{SW}) integrate processes from microphysical to global scales and thus**
80 **are uniquely positioned to track global hydroclimate variations. Here, we evaluate global**
81 **hydroclimate during the past 2,000 years using a globally distributed compilation of**
82 **proxies for δ_{precip} , δ_{MW} , and δ_{SW} . We show that global mean surface temperature exerted a**
83 **coherent influence on global δ_{precip} and δ_{MW} throughout the past two millennia, driven by**
84 **global ocean evaporation and condensation processes, with lower values during the Little**
85 **Ice Age (1450-1850) and higher values after the onset of anthropogenic warming (~1850).**
86 **The Pacific Walker Circulation is a predominant source of regional variability,**
87 **particularly since 1850. Our results demonstrate rapid adjustments in global precipitation**
88 **and atmospheric circulation patterns – within decades – as the planet warms and cools.**

89

90 Recent global syntheses of paleoclimate “proxy” data have constrained global mean surface
91 temperature (GMST) changes during the past 2000 years (i.e., the Common Era, CE), providing
92 critical context for anthropogenic warming^{1,2}. Yet despite the importance of water resources to
93 society, contemporaneous variations in the global water cycle — including precipitation,
94 evapotranspiration, atmospheric circulation, and modes of climate variability that affect these
95 processes — remain underconstrained^{3,4}.

96

97 Stable hydrogen and oxygen isotope ratios ($\delta^2\text{H}$ and $\delta^{18}\text{O}$) in environmental waters are well
98 positioned to provide a global picture of hydroclimate. Evaporation, condensation, freezing, and

99 other phase changes in the water cycle differentially impact (fractionate) heavy versus light
100 isotopes, causing the $\delta^2\text{H}$ and $\delta^{18}\text{O}$ of precipitation (δ_{precip}), precipitation-derived meteoric
101 waters such as lake and soil water (δ_{MW}), and seawater (δ_{SW}) to integrate and record hydrological
102 processes on timescales from minutes to millions of years^{5–12}. Variations in δ_{precip} , δ_{MW} , and δ_{SW}
103 are subsequently incorporated into diverse geologic materials including speleothem and coral
104 carbonate, glacial ice, and tree cellulose. By synthesizing such data from a variety of sources, it
105 is therefore possible to infer changes in a powerful suite of hydroclimatic variables: δ_{precip} , which
106 reflects atmospheric factors such as condensation temperature, precipitation amount, rainout
107 history, and moisture source⁵; δ_{MW} from lake, soil, and groundwaters, which reflects variations in
108 δ_{precip} and surface water evaporation; and δ_{SW} , which reflects δ_{precip} , seawater evaporation, and
109 mixing^{13,14}.

110
111 We analyzed proxies for δ_{precip} , δ_{MW} , and δ_{SW} from the recently published PAGES Iso2k
112 database, which contains 759 globally-distributed paleoclimate records from coral, tree, ice,
113 speleothem, lake, and marine sites¹⁵. The database includes extensive metadata designed to
114 facilitate cross-archive comparison, including interpretations from the original publications and
115 supplemented with information from a team of over 50 archive experts (see ref. ¹⁵ for details on
116 database design). Metadata fields include original climatic interpretations, proxy system
117 transformations, and the multiple environmental drivers of the isotopic composition of the
118 measured material in each record (hereafter “isotope interpretation”). Each record is further
119 classified into one of three primary isotope interpretation groups: 1) δ_{precip} ; 2) Effective Moisture
120 (EM), i.e., the balance between precipitation and evaporation, with higher EM reflecting higher
121 precipitation relative to evaporation; or 3) the *in situ* temperature of the environmental medium

122 during the formation of the proxy sensor or archive¹⁵ (we note most records in the temperature
123 category are marine carbonates whose $\delta^{18}\text{O}$ primarily reflects seawater temperature, with only
124 minor influence of δ_{sw} ¹⁶). Regional and global analyses were performed on these three isotope
125 interpretation groups to distinguish patterns in different reservoirs of the water cycle
126 (precipitation, surface water, seawater), without *a priori* assumptions about the climatic drivers
127 of each record's variability (e.g., upstream monsoon intensity, regional air temperature), which
128 are more subject to change as records are re-interpreted over time (Methods).

129
130 For each group we created composite records of global $\delta^{18}\text{O}$ anomalies relative to the 0–2000
131 mean ($\Delta^{18}\text{O}$), including $\delta^2\text{H}$ records scaled to $\delta^{18}\text{O}$ -equivalent variance, using a dynamic
132 compositing method that was previously employed to reconstruct paleotemperature in a manner
133 that robustly handles proxy timeseries of different lengths, resolutions, and coverage periods (ref.
134 ¹⁷ and Methods). In addition to calculating composites, we performed Principal Component
135 Analysis (PCA) on a subset of higher-resolution (i.e., ≤ 30 year bins) individual proxy records
136 with $>85\%$ temporal data coverage during the Last Millennium (LM; 850–1850) to reveal
137 dominant spatiotemporal modes of variability (Methods). We compared these results to an
138 ensemble of three full-forcing LM experiments with the water isotope-enabled Community Earth
139 System Model (iCESM)^{18–20}.

140
141 The three $\Delta^{18}\text{O}$ composites (Fig. 1) display similar patterns, with notable differences in the
142 magnitude of centennial-scale variability. During the first millennium, composite $\Delta^{18}\text{O}$ of δ_{precip} -
143 driven records (hereafter, composite $\Delta^{18}\text{O}_{\delta_{\text{precip}}}$) was relatively stable, whereas composite $\Delta^{18}\text{O}$
144 of EM- and temperature-driven records (composite $\Delta^{18}\text{O}_{\text{EM}}$ and $\Delta^{18}\text{O}_{\text{temp}}$) increased and

145 decreased, respectively. During the LM, all three composites show a monotonic trend from ~800
146 to ~1700, and a reversal of that trend since the 19th century. These patterns broadly echo the
147 temporal evolution of GMST during the LM¹, but with different magnitudes depending on the
148 primary environmental interpretation of $\delta^{18}\text{O}$. From 1000 to 1850, a global cooling of $0.25 (\pm 0.1)$
149 $^{\circ}\text{C}^{-1}$ corresponds to a change of $-0.27 (\pm 0.00021)$, $+0.02 (\pm 0.00019)$, and $+0.09\text{‰} (\pm$
150 $0.0002)$ in composite $\Delta^{18}\text{O}_{\delta\text{precip}}$, $\Delta^{18}\text{O}_{\text{EM}}$, and $\Delta^{18}\text{O}_{\text{temp}}$, respectively (Fig. 1A-C). Subsequent
151 warming of $0.65 (\pm 0.06)^{\circ}\text{C}$ from 1850 to 2000 corresponds to a change of $+0.56 (\pm 0.00012)$,
152 $+0.62 (\pm 0.00017)$, and $-0.16\text{‰} (\pm 0.00023)$, respectively. Uncertainties in these estimates are
153 based on differences between the respective time periods across the full ensemble (Methods).
154

155 Composite $\Delta^{18}\text{O}_{\text{EM}}$ displays pronounced centennial-scale variability, with distinct positive
156 excursions from 300–500, 700–900, and 1800–2000. Variability in composite $\Delta^{18}\text{O}_{\text{EM}}$ is at least
157 twice the magnitude of composite $\Delta^{18}\text{O}_{\text{temp}}$ or $\Delta^{18}\text{O}_{\delta\text{precip}}$ (Fig. 1), likely due to the strong
158 influence of surface-water evaporation on lake and seawater $\delta^{18}\text{O}$, which amplifies the δ_{precip}
159 signal relative to noise^{5,7}.

160
161 The first principal component (PC1) of each category of records is dominated by a monotonic
162 trend over the LM, with smaller centennial-scale fluctuations (Fig. 2A). Similar to the
163 composites, the gross trend in each PC1 corresponds to a decrease in GMST. Site loadings on
164 each PC1, however, differ by region and by the primary environmental driver of $\delta^{18}\text{O}$ (Fig. 2B-
165 D). For example, positive trends and negative PC1 loadings are evident in $\delta^{18}\text{O}_{\text{temp}}$ at almost all
166 extra-tropical locations (Fig. 2D), consistent with the impact of ocean cooling on the $\delta^{18}\text{O}$ of

167 marine carbonates. Contrastingly, trends are insignificant in the Indo-Pacific Warm Pool where
168 $\delta^{18}\text{O}_{\text{sw}}$ influence likely confounds the temperature signal²¹.

169

170 **Influence of temperature on global δ_{MW}**

171 Together, the $\Delta^{18}\text{O}$ composites and PC1 suggest that GMST exerts a first-order control on
172 temporal changes in global δ_{MW} during the CE. The relationship of composite $\Delta^{18}\text{O}_{\delta\text{precip}}$ with
173 temperature is $0.68 \pm 0.20 \text{ ‰}/^\circ\text{C}$ for the full CE and $0.78 \pm 0.19 \text{ ‰}/^\circ\text{C}$ from 850-2000, based on
174 regression of the 30-year binned values (Methods) (Fig. 1A). A positive relationship between
175 GMST and δ_{precip} may be expected from high latitude ice cores^{22–24}, but positive relationships in
176 composite $\Delta^{18}\text{O}_{\delta\text{precip}}$ persist even when such records are excluded (Extended Data Fig. 1), and
177 also occur at mid and low latitudes, especially after 1850 (Extended Data Fig. 2). In addition to
178 the composites, the positive relationship between δ_{precip} and GMST is evident in PC1 of the δ_{precip}
179 records spanning the entire CE (Extended Data Fig. 3A-B) and in iCESM simulations (Fig.
180 3A,D; Extended Data Fig. 4). In iCESM, the regression slope between GMST and global, 30-
181 year smoothed, mean annual $\delta^{18}\text{O}_{\text{precip}}$ from 850-2000 is $0.25\text{ ‰}/^\circ\text{C}$, and $0.48\text{ ‰}/^\circ\text{C}$ when
182 calculated using Iso2k site locations (which, for δ_{precip} records, excludes nearly all ocean grid
183 cells and regions where site-level regression slopes are close to 0; Extended Data Fig. 4). The
184 iCESM slopes are shallower than in the Iso2k data, but the global slope is consistent with earlier
185 GCM estimates of $0.3\text{ ‰}/^\circ\text{C}$ during the last deglaciation²⁵ and simplified model estimates of
186 zonal-mean temporal slopes of $\sim 0.1\text{--}0.4\text{ ‰}/^\circ\text{C}$ for most latitudes²⁶. The discrepancy between the
187 Iso2k and iCESM temporal slopes may reflect model biases in extratropical moisture transport
188 and positive $\delta^{18}\text{O}_{\text{precip}}$ biases at the high latitudes¹⁸. However, observationally, the global
189 temporal slope between GMST and $\delta^{18}\text{O}_{\text{precip}}$ has not been quantified observationally— unlike

190 spatially-derived slopes between site-level air temperature and $\delta^{18}\text{O}_{\text{precip}}$ ^{23,27,28}— because modern
191 $\delta^{18}\text{O}_{\text{precip}}$ measurements in most regions are either absent or too short and discontinuous (most
192 records <10 years) to do so beyond the scale of a few years^{29,30}. Despite differences in
193 magnitude, both iCESM and Iso2k data demonstrate that a positive relationship between GMST
194 and δ_{MW} is a persistent feature of the global water cycle for the CE. The 30-year-binned Iso2k
195 temporal slope of $0.68 \pm 0.20 \text{ ‰/°C}$ should be considered a benchmark to be tested as longer
196 observations and reanalyses become available.

197

198 Ice core and marine sediment studies have long recognized the importance of air temperature in
199 driving high latitude δ_{MW} , and of global ice volume in driving global δ_{SW} , on glacial-interglacial
200 timescales and across the Cenozoic^{24,26}. However, the nature of this relationship has remained
201 uncertain on the shorter (decadal to centennial) timescales most relevant for understanding
202 modern climate change and its impacts on water resources. Our results provide the first
203 observational evidence that GMST drives temporal changes in δ_{MW} and δ_{SW} , and therefore
204 changes in the hydrological cycle, on such timescales. Mechanisms other than global ice volume,
205 which has not changed substantially during the CE, are therefore required to explain this
206 relationship.

207

208 Although the Iso2k analyses are the first to document it, stable isotope theory and experimental
209 studies provide ample foundation for a positive imprint of GMST on global δ_{MW} , which is what
210 our spatially-distributed (albeit not spatially continuous) proxy network approximates. At the
211 global scale, a relationship between δ_{MW} and GMST will integrate all processes that relate local-
212 scale δ_{MW} with GMST, while balancing out regional distributions of heavy vs. light

213 isotopologues throughout the water cycle. Variations in global δ_{MW} therefore reflect variations in
214 the isotopic composition of the global oceanic and atmospheric reservoirs. Atmospheric δ_{vapor} is
215 ultimately governed by the isotopic composition of water evaporated from the oceans.
216 Equilibrium fractionation is greater at lower temperatures²⁷, so in a cooler world, the liquid-to-
217 vapor difference in $\delta^{18}O$ is higher than in warmer conditions (i.e., lower δ_{vapor} in the saturated
218 atmospheric layer above the ocean surface). Kinetic fractionation further decreases atmospheric
219 δ_{vapor} as newly evaporated vapor diffuses and mixes into the undersaturated free atmosphere,
220 with stronger fractionation when the lower troposphere is less humid^{28,29}. A globally cooler and
221 drier troposphere should therefore decrease δ_{vapor} to a greater extent than a warmer and more
222 humid troposphere. Global δ_{vapor} is further modified by temperature-dependent fractionation as
223 precipitation forms and condensation preferentially removes ^{18}O and decreases δ_{vapor} , with
224 greater isotopic discrimination at colder condensation temperatures^{27,30}.
225
226 iCESM simulations indicate multiple mechanisms play a role (Fig. 3). Higher GMST is
227 associated with higher $\delta^{18}O$ of water vapor flux from evaporating seawater into the saturated
228 boundary layer (0.14‰/°C), following the Craig-Gordon model^{13,31}, slightly higher relative
229 humidity with respect to sea surface temperature (0.77‰/°C) (Methods), and ultimately, higher
230 atmospheric $\delta^{18}O_{vapor}$ (0.30‰/°C). Global δ_{precip} therefore reflects not only the δ_{vapor} determined
231 during ocean evaporation and mixing into the free atmosphere, but also the subsequent depletion
232 of ^{18}O in atmospheric vapor in the atmosphere through condensation, which via equilibrium
233 fractionation is stronger in a cooler climate. Stronger depletion of heavy isotopes in precipitation
234 also occurs with more vigorous circulation and shorter residence time of atmospheric moisture³².
235 For precipitation integrated over the timescales of most proxy systems (weeks to months), δ_{precip}

236 could become even lower when global precipitation rates are high relative to the amount of
237 precipitable water in the atmosphere, and higher when atmospheric humidity increases to a
238 greater extent than precipitation rate, as in the 20th century (Fig. 3; ref. ³³).

239

240 Theory and simplified model experiments suggest that a cooler global atmosphere could also
241 favor stronger latitudinal gradients in δ_{precip}^5 , as lower temperatures increase distillation along the
242 water's path from the subtropics to the poles^{23,34}. A cooler atmosphere may also shift evaporative
243 source regions equatorward, driving a greater fraction of high latitude precipitation to be sourced
244 remotely³⁵ which strongly affects δ_{precip} at those latitudes³⁶. The latitudinal gradient in Iso2k
245 δ_{precip} records between 40° to 70° N and S is approximately -0.48‰ per degree latitude, in
246 agreement with observed modern slopes of \sim -0.3 to -0.6‰ per degree latitude^{23,34}. However, we
247 observe no difference in this gradient between the Little Ice Age and the 20th century — the
248 globally coldest and warmest intervals of the CE, respectively^{1,37} (Extended Data Fig. 5). Hence,
249 either equator-to-pole Rayleigh distillation is counterbalanced by changes in spatial patterns of
250 global evaporative recharge and moisture transport relative to precipitation^{35,36}, or the spread in
251 Iso2k δ_{precip} records is too large to resolve changing gradients during the LM when temperature
252 changes are relatively small. As spatial gradients are averaged out at the global scale, further
253 experiments with both simplified models and isotope-enabled GCMs are needed to quantitatively
254 decompose the relative importance of ocean evaporation, condensation, and global precipitation
255 and evaporation patterns on the global-scale GMST- δ_{precip} relationship.

256

257 **Patterns of regional variability**

258 Despite its influence on global mean δ_{MW} , GMST explains neither the spatial patterns nor the
259 shorter-term variability in δ_{MW} and δ_{SW} (Fig. 2, Extended Data Fig. 6). Instead, site-level PC1
260 loadings, LM trends, and centennial anomalies in $\delta^{18}\text{O}_{\delta\text{precip}}$ and $\delta^{18}\text{O}_{\text{EM}}$ are spatially
261 heterogeneous (Figs. 1-2, Extended Data Fig. 7). Although non-climatic processes and noise
262 likely contribute to this variability, this result also indicates that regional water balance,
263 atmospheric circulation, and precipitation characteristics dominate regional δ_{MW} not just in the
264 late 20th/early 21st centuries^{38,39} but also on multi-decadal to millennium-long timescales. In the
265 Arctic and the tropical Andes, negative trends in $\delta^{18}\text{O}_{\delta\text{precip}}$ and positive PC1 loadings agree with
266 documented Little Ice Age climate changes: high-latitude cooling, which lowered δ_{precip} in the
267 Arctic⁴⁰, and intensification of the South American summer monsoon, which lowered δ_{precip} in
268 the Andes⁴¹. In eastern China and the Maritime Continent, positive PC1 loadings and negative
269 trends in $\delta^{18}\text{O}_{\delta\text{precip}}$ and $\delta^{18}\text{O}_{\text{EM}}$ over the LM indicate increasing effective moisture, with
270 depletion of heavy isotopes at some sites enhanced by intensifying convection and moisture
271 transport within the East Asian and Australasian summer monsoons^{42,43}. In northwestern North
272 America and Central America, negative PC1 loadings and positive trends in $\delta^{18}\text{O}_{\delta\text{precip}}$ and
273 $\delta^{18}\text{O}_{\text{EM}}$ indicate increasing $\delta^{18}\text{O}_{\text{MW}}$ and declining EM over the LM, while southwestern North
274 America shows the opposite pattern, consistent with other LM proxy reconstructions^{44,45}. $\delta^{18}\text{O}_{\text{EM}}$
275 from lakes exhibit the clearest trends in western North America, likely because δ_{precip} in the
276 western North American interior is especially sensitive to changes in water balance³⁹ and
277 enhanced evaporation during dry periods then amplifies increases in lake water $\delta^{18}\text{O}$. This
278 explains why coherent patterns emerge in western North American isotopic proxy records
279 despite substantial heterogeneity in compilations that blend isotopic and non-isotopic records⁴⁵.
280

281 Opposing precipitation anomalies between southwestern North America and Central Asia versus
282 the Maritime Continent and South Asia during the LM have previously been attributed to
283 variability in the El Niño-Southern Oscillation⁴⁶, the interannual component of the east-west
284 atmospheric overturning circulation over the tropical Pacific known as the Pacific Walker
285 Circulation (PWC)⁴⁷. An underlying influence of the PWC may also explain some of the regional
286 coherency in Iso2k δ_{MW} . In modern precipitation, strengthening and weakening of the PWC
287 drives opposing precipitation and $\delta^{18}\text{O}_{\text{precip}}$ anomalies in Asia and the Americas due to changes
288 in precipitation amount, moisture source, and transport pathways³⁸. For example, rerouting of the
289 jet stream during El Niño events alters Pacific Ocean moisture trajectories toward southwestern
290 rather than northwestern North America^{48,49}. To the extent that these relationships persist beyond
291 interannual timescales, changes in moisture transport and EM provide a plausible mechanism for
292 multidecadal to centennial patterns in Asian and western North American $\delta^{18}\text{O}_{\text{EM}}$.

293

294 Evidence for the PWC's influence on Iso2k records is stronger on sub-decadal timescales during
295 the historical period (1850–2005), when instrumental observations are available for direct
296 comparison. We correlated PC1 of 3-year binned Iso2k EM records with observed sea level
297 pressure (SLP) and found that the associated pattern mimics the observed global expression of
298 the PWC (Fig. 4a). Similarly, in iCESM experiments, PC1 of soil water $\delta^{18}\text{O}$ ($\delta^{18}\text{O}_{\text{soil}}$) at Iso2k
299 EM sites displays an SLP pattern that resembles iCESM's PWC (Fig. 4b). There is vigorous
300 debate surrounding the extent to which the PWC fluctuates on multidecadal and longer
301 timescales, either due to internal variability in the climate system or to external forcing^{50–52}. Our
302 results suggest that the PWC was the predominant influence on interannual $\delta^{18}\text{O}_{\text{precip}}$ not only

303 from 1982 to 2015³⁸, but at least since 1850, and likely on multi-decadal timescales prior to
304 1850.

305

306 Our results reveal a remarkably consistent relationship between GMST and δ_{MW} throughout the
307 CE, despite relatively constant ice-ocean boundary conditions. Between 1850-2000, global δ_{precip}
308 increased by at least 0.56‰, indicative of a warmer, more humid troposphere. Global δ_{MW} and
309 regional δ_{MW} appear to adjust to changing temperature and atmospheric circulation patterns,
310 respectively, within decades – similar to the timescale of the forcing itself. Expanded δ_{MW}
311 observational networks are critical for detecting and attributing shifts in rainfall, drought, and
312 circulation as the planet continues to warm.

313

314 **Acknowledgments**

315 Iso2k is a contribution to Phase 3 and 4 of the PAGES 2k Network. PAGES received support
316 from the Swiss Academy of Sciences, the US National Science Foundation, and the Chinese
317 Academy of Sciences. We thank three anonymous reviewers for helpful comments which
318 improved this manuscript.

319

320 Support for this work includes NSF-AGS grant 1805141, NSF-AGS PRF 1433408, and a David
321 and Lucile Packard Foundation Fellowship in Science and Engineering to Bronwen L. Konecky.
322 Samantha L. Stevenson was supported by NSF-AGS grant 1805143. Georgina M. Falster was
323 supported by NSF-AGS grant 1805141 to B. Konecky and by the Australian Research Council
324 Centre for Excellence for Climate Extremes (CE170100023). Jessica Conroy was supported by
325 NSF-CAREER-1847791. Diane M. Thompson was supported by NSF-CAREER-1945479, NSF-

326 1931242, and NSF-2002460. Lukas Jonkers was funded through PalMod, the German
327 paleoclimate modeling initiative. PalMod is part of the Research for Sustainable Development
328 initiative funded by the German Federal Ministry of Education and Research (BMBF). Olga
329 Churakova (Sidorova) was supported by RSF project 21-17-00006. Kristine DeLong was
330 supported by South Central Climate Adaptation Science Center Cooperative Agreement
331 G19AC00086. Belen Martrat (BM) was funded by the RYC-2013-14073 programme and the
332 LINKA20102 and CEX2018-000794-S projects. Jonathan Tyler was supported by the Australian
333 Research Council Discovery Project DP190102782. Nerilie J. Abram was supported by the
334 Australian Research Council through a Future Fellowship (FT160100029), Special Research
335 Initiative for the Australian Centre for Excellence in Antarctic Science (SR200100008) and the
336 Centre of Excellence for Climate Extremes (CE170100023).

337

338 **Author contributions**

339

340 Analyses presented in the main text and extended data were conceived and performed by BLK,
341 NPM, GMF, SS, MJF, AA, DMT, MDJ, JJT, EKT, JLC, SGD, and LJ.

342

343 Results were analyzed and interpreted by BLK, NPM, GMF, SS, MJF, AA, DMT, MDJ, KLD,
344 JJT, BM, and EKT, with input from all authors.

345

346 The manuscript was written mainly by BLK, NPM, GMF, SS, MJF, AA, DMT, MDJ, KLD, JJT,
347 BM, EKT, JLC, SGD, LJ, and HRS, with additional contributions from OVC, ZK, TO, TJP, and
348 GS.

349

350 All Iso2k Project Members created the Iso2k database and edited the manuscript.

351

352 BLK directed the project, led the overall design of the study, and led the writing of the
353 manuscript.

354

355 **Competing interests:**

356

357 The authors declare no competing interests.

358

359

360 **Figure legends/captions**

361 **Fig. 1. Global composite $\delta^{18}\text{O}$ anomalies. a-c**, 30-year binned proxy $\Delta^{18}\text{O}$ (black line, ensemble
362 median; dark shading, 25th–75th percentiles; light shading, 2.5th–97.5th percentiles) for each group
363 of Iso2k records¹⁵, anomalies relative to 2000-year mean. Gray shading depicts ensemble 2.5th–
364 97.5th percentile GMST anomaly relative to 1961-1990 mean¹. Note y-axis in (c) is reversed to
365 orient values upwards for warmer periods. **d-f**, Records contributing to each composite. Symbol
366 shape, archive type; size, record duration; shading, correlation between that record and the
367 corresponding composite; bold outline, $p < 0.05$. Correlations are Pearson's r , two-sided, with no
368 adjustment for multiple correlation. Maps created in R, using coastlines from Natural Earth.

369

370

371 **Fig. 2. First principal components and trends in Iso2k records over the Last Millennium. a**,
372 PC1 of 30-year binned Iso2k records¹⁵ (850 to 1840), by interpretation group (colored lines),
373 compared to GMST anomaly (gray shading) as in Fig. 1. **B-d**, Spatial loadings on PC1 (symbol
374 shading) for each group. Correlations are Pearson's r , two-sided, with no adjustment for multiple
375 correlation. Inner symbols, archive type; outer symbol shape, slope of significant ($p < 0.05$) linear
376 trend in the $\delta^{18}\text{O}$ of each individual record; labels, variance explained by PC1 and number of
377 records used. Maps created in R, using coastlines from Natural Earth.

378

379 **Fig. 3. Global hydroclimate and isotopic anomalies in iCESM¹⁵. A**, Ensemble mean, amount-
380 weighted mean annual $\Delta^{18}\text{O}_{\text{precip}}$ anomaly relative to 1961 to 1990 mean (thin gray line) and 30-
381 year running mean (thick black line) for all grid cells, and for only grid cells containing Iso2k
382 site locations (blue lines). Note right Y axis in a is scaled 2x that of the left. **B-f**, as in a, but for

383 (b) global column-averaged $\Delta^{18}\text{O}_{\text{vapor}}$, (c) $\Delta^{18}\text{O}$ of evaporative flux from the global oceans, (d)
384 GMST, (e) relative humidity over the low- and mid-latitude oceans (60°N-60°S), with respect to
385 saturation vapor pressure at sea surface temperature^{13,28,29}, and (f) global precipitation rate.

386

387 **Fig. 4. Isotopic fingerprint of the Pacific Walker Circulation in Iso2k¹⁵ and iCESM. a,**
388 Shading is the correlation between observed SLP and PC1 of 3-year binned Iso2k EM records
389 (1850 to 2005). Symbol colors denote site loading on PC1. Unfilled contours denote correlation
390 between SLP and PWC index ΔSLP . **b,** Correlation between SLP and ensemble-mean PC1 of 3-
391 year binned 0-10 cm $\delta^{18}\text{O}_{\text{soil}}$ in iCESM experiments (1850 to 2005), using grid cells of Iso2k EM
392 sites (symbols). **c,** As in **b**, but for 30-year binned data from 850-1850. **d-f,** Time series of PC1
393 (black line) and ΔSLP (gray line) corresponding to panels **a-c**. Maps created in MATLAB using
394 `m_map` for coastlines.

395

396 Methods

397 **Disaggregation of analyses by isotope interpretation**

398 All global analyses presented in this paper are disaggregated by isotope interpretation rather than
399 by the original authors' climatic interpretation. This approach avoids building into our synthesis
400 *a priori* assumptions about the specific climatic variable driving $\delta^{18}\text{O}$ and $\delta^2\text{H}$ variability in each
401 record, the basis for which is not always explained in the original publications. In addition, many
402 records contain multiple climatic interpretations (e.g., speleothem $\delta^{18}\text{O}$ being driven mainly by
403 monsoonal rainfall amount, but amplified by the ratio of summer vs. winter moisture source
404 changes¹⁻³), and the relative importance of each variable was impossible to objectively evaluate
405 for every time scale, region, and proxy system in the database. Finally, climatic interpretations of

406 isotope-based proxy records are continually evolving as new information emerges from
407 environmental monitoring and modeling studies (e.g., moisture source and transport
408 characteristics driving Greenland ice core $\delta^{18}\text{O}$ variability⁴⁻⁸; seawater $\delta^{18}\text{O}$ driving coral $\delta^{18}\text{O}$ in
409 some regions⁹). The isotope interpretation groupings are less subject to interpretation because
410 they chiefly represent isotope systematics and the physical pools of environmental waters that
411 each proxy sensor imbibes.

412

413 We separated δ_{precip} and EM records because EM proxies integrate information about evaporation
414 that is not expected from pure δ_{precip} proxies, which are mainly driven by factors influencing
415 condensation (e.g. air temperature, degree of rainout, import of moisture from different
416 sources)^{10,11}.

417

418

419 **Calculation of $\Delta^{18}\text{O}$ composites**

420 All records were extracted from the PAGES Iso2k Database v 1.0.0^{15,53}. The database contains
421 metadata on the principal determinants of isotopic composition in the measured material (e.g.,
422 the $\delta^{18}\text{O}$ of precipitation that forms glacial ice or cave dripwaters) and the record's climatic
423 interpretation (e.g., atmospheric temperature at condensation level, rainout due to monsoon
424 intensity), as interpreted by the original studies' authors and our team of archive experts¹⁵. For
425 each isotope interpretation group, we calculated an ensemble of 100 composite $\delta^{18}\text{O}$ time series
426 for the CE. Prior to calculation, we filtered the database to only include the 'primary' time series
427 for each site, and then grouped records according to the primary driver of isotopic variability i.e.,

428 EM, temperature, or δ_{precip} ^{15,53}) (entitled ‘EffectiveMoisture’, ‘Temperature’, and ‘P_isotope’ in
429 the ‘isotopeInterpretation1_variableGroup’ metadata field of the Iso2k database).

430

431 For records with isotope interpretation ‘P_isotope’, we also calculated separate composites for a)
432 glacier ice only, and b) excluding glacier ice (Extended Data Fig. 1). This separation was
433 performed to assess whether composite $\Delta^{18}\text{O}_{\delta_{\text{precip}}}$ is overprinted by the large number of ice core
434 records from high latitudes and high elevations, where temperature-driven isotopic fractionation
435 may disproportionately affect δ_{MW} ¹². An especially strong temperature- δ_{MW} relationship may be
436 unsurprising in the glacier ice $\delta^{18}\text{O}$ system. Glacier ice reflects δ_{precip} more directly than other
437 proxy sensors, which reflect pools of meteoric water (e.g. soil water and lake water) that are
438 influenced by precipitation and other secondary processes such as evaporation or aquifer
439 mixing. Glacier ice is found at high latitudes and altitudes, where cold temperatures drive
440 stronger stable isotope fractionation due to Rayleigh distillation and global patterns of
441 precipitation vs. evaporative recharge^{5-7,13-15}. Most of the glacier ice records included in the
442 Iso2k database are consistently interpreted as temperature indicators, and were included in the
443 PAGES 2k^{12,16} temperature database used for GMST calculations.

444

445 Despite these considerations, the observed global δ_{MW} -temperature relationship persists even
446 when glacier ice records are removed from the δ_{precip} composite (**Extended Data Fig. 1**), and in
447 low- and mid-latitudes where local temperature effects on δ_{precip} are small¹³ (**Fig. 2**). The overall
448 patterns in PC1 are also similar regardless of whether glacier ice records are included or
449 excluded (**Extended Data Figs. 3, 8**). Therefore, the inclusion or exclusion of glacier ice records
450 does not substantially affect the composites or PCA, supporting that the strong temperature- δ_{MW}

451 relationship in our data is due to the overall influence of temperature on the global pool of
452 meteoric water and not due to the strong effect of air temperature on high-latitude ice cores.

453

454 Records with ten or fewer data values within the CE were excluded from the analysis. $\delta^2\text{H}$
455 records ($n=45$ in composite $\Delta^{18}\text{O}_{\delta\text{precip}}$, $n=12$ in composite $\Delta^{18}\text{O}_{\text{EM}}$) were divided by eight to
456 scale the magnitude of their variance with that of $\delta^{18}\text{O}$ in global meteoric waters⁵⁴. This was
457 done to avoid erroneously high apparent climate variability at $\delta^2\text{H}$ sites simply from the eight-
458 times-higher variability in $\delta^2\text{H}$ relative to $\delta^{18}\text{O}$, which arises from relative differences in
459 equilibrium fractionation factors between liquid and vapor for these isotope ratios⁵⁴. Local slopes
460 were not available for the 12 records from evaporative water bodies in composite $\Delta^{18}\text{O}_{\text{EM}}$, so the
461 global scaling of 8 was used.

462

463 Records in the Iso2k database have a wide variety of temporal resolution, length, and coverage
464 over the CE¹⁵. To align records to a common interval and resolution, the data were averaged into
465 equal bins of 30 years spanning the CE, which approximates the average resolution of the lower
466 resolution archive types in the database (marine and lake sediments). Records contributing to
467 each bin were mean-centered but not scaled by variance, as described below. To minimize
468 aliasing, the data were binned following a modified nearest-neighbor annual interpolation
469 procedure¹⁷. This approach accounts for the fact that for the non-annually-resolved data, the age
470 of a sample at a given depth typically represents more than one year of accumulation (and up to
471 several years or decades, or even longer for some low-resolution sedimentary records), and may
472 therefore contain climate information that is relevant to more than one bin. The duration of each
473 sample is not consistently recorded in the Iso2k database (or the primary references), so to

474 estimate sample coverage we calculated the distribution of gaps between adjacent observations in
475 each timeseries, and used nearest-neighbor interpolation to estimate sample values spanning the
476 intervals that are less than the 75th quantile of the distribution of all gaps between adjacent
477 observations (consistent with Kaufman et al.¹⁷). Consequently, samples with resolution <30
478 years can potentially contribute to the weighted $\delta^{18}\text{O}$ calculation for up to two bins, though with
479 less weight given to samples further from their published age. In the case of records with
480 resolution >30 years, this data-spreading step allows observations to impact the composites
481 across multiple bins, consistent with their interpretation as multidecadal averages.

482

483 Record lengths also vary widely in the database, so there is no universal time period of common
484 overlap within the CE. We therefore aligned the records using the Dynamic Compositing
485 approach¹⁷, which uses randomly selected portions of each time series to adjust the $\delta^{18}\text{O}$
486 variance, then iteratively adjusts the mean $\delta^{18}\text{O}$ of each time series so that the mean of each
487 record is minimally offset from all other records in the composite. This process was repeated for
488 each of 100 ensemble members. Because the mean value of the records is adjusted during
489 compositing, the composite values are now in relative $\Delta^{18}\text{O}$ (in ‰), rather than in their original
490 $\delta^{18}\text{O}$ (or pre-scaled $\delta^2\text{H}$) values on the VSMOW-SLAP scale (i.e., in $1000 \cdot \delta$ notation where 0‰
491 refers to standard mean ocean water). Therefore, for convenience, composite $\Delta^{18}\text{O}$ was slightly
492 shifted such that the mean of the ensemble median is 0‰. The final composite $\Delta^{18}\text{O}$ values (**Fig.**
493 **1**) are therefore in units of ‰ anomalies relative to the 2000-year mean. Dynamic compositing
494 was used in ref. ¹⁷ to produce calibrated reconstructions of paleotemperature. Unlike surface air
495 temperature observations, long and complete timeseries of globally distributed δ_{precip} , δ_{MW} , and
496 δ_{sw} observations are insufficient (e.g. for δ_{precip} , large spatial coverage gaps and few records

497 longer than 10 years³⁸), and so calibrated reconstructions are not possible until these
498 observational networks are improved.

499

500

501

502 **PCA of Iso2k data**

503 We used PCA to calculate Empirical Orthogonal Functions (EOFs) from a subset of records in
504 the Iso2k database that met requirements for temporal coverage (described below; Fig. 2). Prior
505 to calculating the EOFs, we filtered the database as described for the $\Delta^{18}\text{O}$ composites, and
506 binned the raw data. PCA was performed using records in each of the three “isotope
507 interpretation” categories; for ‘P_isotope’ records, we performed separate PCA for a) glacier
508 ice, and b) ‘not glacier ice’ (i.e., all P_isotope records that are not from glacier ice). PCA was
509 performed on three temporal subsets: 0-1980 CE (30-year bins), 850-1840 (30-year bins), and
510 1850-2005 (3-year bins). Here we describe the methodology for the 850-1840 PCA that is shown
511 in the main text, then outline any adaptations that were made for the other two intervals.

512

513 Prior to PCA, all records were truncated to a fixed time interval of 850-1840. Other time
514 windows were explored and are presented in Extended Data Figs. 3 and 8. The 850-1840 interval
515 was chosen in order to focus on pre-industrial variability, to avoid issues with records or
516 chronologies not extending fully to either the present day or the start of the CE, and to provide
517 comparison with LM model experiments from 850-1850. (Note a 990-year interval was used
518 because it is divisible by the 30-year bin size). Results of PCA on the 0-1980 interval (with 30-

519 year bins) and 1850-2005 (with 3-year bins) are shown in Extended Data Figs. 3 and 8. All data
520 processing for these intervals was as below.

521

522 Records included in the PCA had to meet stricter time coverage and completeness requirements
523 than records included in the composites. Binned records with <85% temporal coverage during
524 the 850-1840 interval were excluded. EOF analysis was carried out on the matrix of remaining,
525 screened time series using the Data Interpolation Empirical Orthogonal Function (DINEOF)
526 method, which accounts for records with a small number of missing data points^{55,56}. DINEOF
527 performs best when missing values are scattered randomly throughout the input data time series.
528 In the case of Iso2k records, missing data are generally concentrated at the ends of records, and
529 hence records with a large proportion of missing data have a large impact on the PC loadings
530 (though less impact on the overall PC time series). To check for obvious artifacts induced by the
531 data processing, we visually compared the binned and interpolated records with their raw data
532 equivalents. We performed the PCA on the binned and interpolated data matrix using the `rda()`
533 function of the ‘vegan’ package in R⁵⁷. We scaled the interpolated records to unit variance
534 because they are from different proxy systems and hence the raw data have widely ranging
535 variance.

536

537 To test whether variability explained by the principal components could be explained
538 stochastically, we tested the magnitude of the eigenvalues against a stochastic null hypothesis,
539 using a block bootstrap method that accounts for decadal persistence (Extended Data Fig. 9). For
540 the 850-1840 analysis, we split all raw data records that contributed to the EOF into ten-year
541 blocks; we chose ten years because this separates interannual variance from interdecadal

542 persistence. For each time series, we randomly selected an initial block, identified all blocks with
543 similar means, and randomly sampled one block from these. The next selected block was the
544 successor to that randomly sampled block. Blocks with similar means were identified using
545 nearest neighbor-based ranking. For blocks with no successor (i.e., where there is a gap in the
546 time series), the successor block was randomly selected from all other blocks. The process was
547 then repeated 1000 times to produce an ensemble of time series. This method of re-sampling
548 preserves the effects of 1) irregular time spacing, 2) the autocorrelation function (to lags >30
549 years), and 3) the time series processing steps (e.g., binning) on the correlation structure of the
550 raw (unprocessed) time series. We followed exactly the same steps for the 0-1980 PCA, using a
551 30-year bin size.

552

553 The 1850-2004 PCA was performed using three-year bins, on records with 80% coverage. Block
554 bootstrap was performed using 3-year blocks because 10-year blocks were too coarse for this
555 short time period. As with the above, records were binned and standardized but not detrended.

556

557 **PCA with iCESM experiments**

558 To compare the iCESM with Iso2k results, we performed PCA of 30-year binned iCESM surface
559 soil water $\delta^{18}\text{O}$ ($\delta^{18}\text{O}_{\text{soil}}$) i.e. the model variable most comparable to evaporation-sensitive
560 systems such as lakes. We used data from Iso2k EM site locations, spanning 850-1850, and then
561 regressed the ensemble-mean first PC against model SLP. The binned $\delta^{18}\text{O}_{\text{soil}}$ was calculated for
562 gridpoint time series corresponding to the “effective moisture” sites, taken from each isotope-
563 enabled Last Millennium Ensemble full-forcing ensemble member from the upper 0-10 cm of the
564 soil profile in iCLM, then averaged to produce an ensemble mean. The upper 10 cm were chosen

565 because in the model, isotopic fractionation is clearest at this level whereas $\delta^{18}\text{O}_{\text{soil}}$ of deeper soil
566 layers rapidly approaches $\delta^{18}\text{O}_{\text{precip}}$ ^{18,58}. EOF analysis was performed using $\delta^{18}\text{O}_{\text{soil}}$ because the
567 “lake” land cover type in iCLM4 is non-fractionating^{18,58} and hence no model variable is
568 available for direct comparison with the large number of lake-based Iso2k $\delta^{18}\text{O}_{\text{EM}}$ proxies. Yet to
569 first order, $\delta^{18}\text{O}_{\text{soil}}$ is similarly controlled by both $\delta^{18}\text{O}_{\text{precip}}$ and surface evaporation, and $\delta^{18}\text{O}_{\text{soil}}$
570 is also an adequate comparison to tree cellulose and speleothem records in the Iso2k EM
571 category.

572

573 **Correlations with sea level pressure and calculation of PWC index**

574 Observed SLP and ΔSLP for the correlations against Iso2k HP PC1 (Fig. 4) were taken from the
575 HadSLP2r dataset⁵⁹. Following the treatment of the Iso2k data, the HadSLP dataset was binned
576 to 3 years but not detrended or deseasonalized (Fig. 4).

577

578 The index for the trans-Pacific SLP gradient (ΔSLP) is defined as anomalies (from the monthly
579 climatology) in the difference between area-mean SLP over the central-eastern Pacific Ocean
580 (160°W - 180°W , 5°S - 5°N) and the western Pacific and eastern Indian Oceans (80°E - 160°E , 5°S -
581 5°N)⁵². Positive ΔSLP values represent an increased zonal pressure gradient, and hence stronger
582 PWC (and vice versa). ΔSLP was calculated using HadSLP2r for comparisons with Iso2k (Fig.
583 4).

584

585 **Magnitudes of change in composite $\Delta^{18}\text{O}$ and GMST**

586 To estimate the magnitude of change in the three composite $\Delta^{18}\text{O}$ time series, we subtracted the
587 composite $\Delta^{18}\text{O}$ value at 1000 CE from the composite $\Delta^{18}\text{O}$ value at 1850 CE, for all 100

588 composite ensemble members. We likewise calculated the difference between 2000 CE and 1850
589 CE. Similarly for estimating the change in GMST during this interval, we subtracted the
590 temperature anomaly at 1000 (1850) from the same at 1850 (2000), for all 7000 ensemble
591 members. In all cases, we report the mean and standard deviation of the distributions of
592 magnitudes of change.

593

594 **Calculation of isotope-temperature relationships in Iso2k data and iCESM experiments**

595 We calculated the relationship between composite $\Delta^{18}\text{O}_{\delta\text{precip}}$ (i.e., an approximation of
596 anomalies in the global mean $\delta^{18}\text{O}$ of precipitation, given the spatial distribution of 305
597 δ_{precip} -sensitive proxy records) and GMST between 850-2000. We binned all ensemble
598 members from the most recent reconstruction of CE GMST1 to match the $\Delta^{18}\text{O}_{\delta\text{precip}}$
599 composite. We then calculated linear regressions for 10000 unique combinations of
600 composite $\Delta^{18}\text{O}_{\delta\text{precip}}$ ensemble member ($n = 100$) on GMST ensemble member ($n = 7000$),
601 for the two time intervals. We report the mean and standard deviation of the distribution of
602 regression coefficients, for the two time intervals.

603

604 For iCESM, isotope/temperature relationships were calculated for 850-2000 (the period of
605 overlap with Iso2k composites) using area-weighted globally averaged, mean annual
606 surface temperature and area-weighted, amount-weighted, mean annual global average
607 $\delta^{18}\text{O}_{\text{precip}}$ from the ensemble-mean of three isotope-enabled Last Millennium Ensemble
608 full-forcing simulations. Before determining the regression slopes, we calculated 30-year
609 running means for both surface temperature and $\delta^{18}\text{O}_{\text{precip}}$ (Fig. 3). Regression slopes in the
610 main text are reported for GMST vs. two time series: global mean $\delta^{18}\text{O}_{\text{precip}}$ (using all grid

611 cells), and mean $\delta^{18}\text{O}_{\text{precip}}$ calculated only for grid cells containing locations of Iso2k
612 primary time series data contributing to the composites between 850-2000 CE.

613

614 Similarly, to estimate the amount of variance in individual Iso2k primary time series explained
615 by proxy estimates of global temperature (Extended Data Fig. 6), we calculated R^2 for the 30-
616 year binned data across the interval 1-2000, ignoring bins that contained no observations.

617 Correlations were only calculated if at least six bins overlapped the bins from the GMST
618 reconstruction.

619

620 **Calculation of Relative Humidity normalized to SST**

621 Relative humidity was calculated from iCESM experiments for all grid points over the oceans
622 from 60°N-60°S, i.e. the portion of the lower troposphere receiving the majority of evaporated
623 water from the surface oceans. RH_{SST} in Fig. 3 was calculated as the relative humidity of the
624 surface-most model layer, normalized to the saturation vapor pressure at the temperature of the
625 surface ocean rather than the air, following the physical principles of the Craig-Gordon model
626 for an evaporating water body^{13,28,29}. All global-mean time series in Fig. 3 are area-weighted.

627

628 **Calculation of trends**

629 Trends (Fig. 2) were calculated as the slope of the linear regression from 850-1840 for a subset
630 of Iso2k records meeting the following criteria: 1) designated ‘primary time series’, 2)
631 containing at least one data point in the first and last 50 years of the time interval; and 3)
632 containing at least 20 data points over the full time interval (i.e., ≥ 50 year average resolution).

633 For iCESM data, trends were calculated as the slope of the linear regression for monthly data
634 covering the 850-1850 and 1850-2005 time intervals.

635

636 **200-year standardized anomalies**

637 We created standardized anomaly ('z score') maps to aid interpretation of temporal variability in
638 the composite time series (Extended Data Fig. 7). Similarly to the analyses described above, we
639 filtered the database to only include the 'primary' isotope ($\delta^{18}\text{O}$ or $\delta^2\text{H}$) time series for each site,
640 and then grouped records according to the primary driver of isotopic variability. We then filtered
641 this subset of data sets to only include records spanning >600 years within the CE. We averaged
642 those records into 200-year bins, and then calculated z-scores for each bin by subtracting the
643 mean of all data points within the CE from the bin average, and then dividing by the standard
644 deviation of all data points within the CE. We performed this analysis using both 'odd' (100,
645 300, 500 etc.) and 'even' (200, 400, 600) centuries as bin centers and showed only the time
646 periods relevant to the main text in Extended Data Fig. 7.

647

648 **Data Availability Statement**

649 The Iso2k Database⁵³ is available for download at <https://doi.org/10.25921/57j8-vs18> and is

650 accessible via the NOAA/WDS Paleo Data landing page at

651 <https://www.ncdc.noaa.gov/paleo/study/29593>. Composites and principal components datasets

652 generated for this manuscript are available through NOAA/NCEI.

653

654 **Code Availability Statement**

655 Codes to reproduce the results from this manuscript are available via Github

656 <https://github.com/nickmckay/iso2kNatureGeoscience2023> and archived on Zenodo.

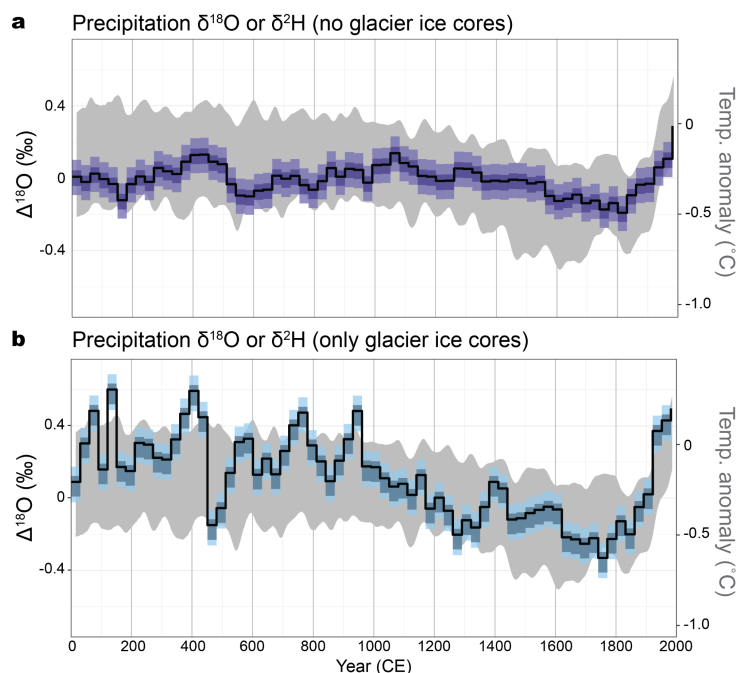
657

658

659

EXTENDED DATA FIGURES 1-9

660



661

662 **Extended Data Figure 1. Composite $\Delta^{18}\text{O}_{\delta\text{precip}}$ calculated with and without glacier ice**

663 **records.** As per Fig. 1, the black line with coloured shading shows the 30-year binned proxy

664 $\delta^{18}\text{O}$ anomaly from Iso2k records¹⁵ (black line, ensemble median; dark shading, first and third

665 quantiles; light shading, 2.5th/97.5th percentiles). **(a)** Composite of $\Delta^{18}\text{O}_{\delta\text{precip}}$ records from all

666 archives other than glacier ice. **(b)** Composite of only glacier ice records. Records contributing

667 to each bin are mean-centered but not scaled according to that record's variance (see Methods).

668 Anomalies are in ‰ relative to the 2000-year mean. Gray shading depicts the ensemble 2.5 and

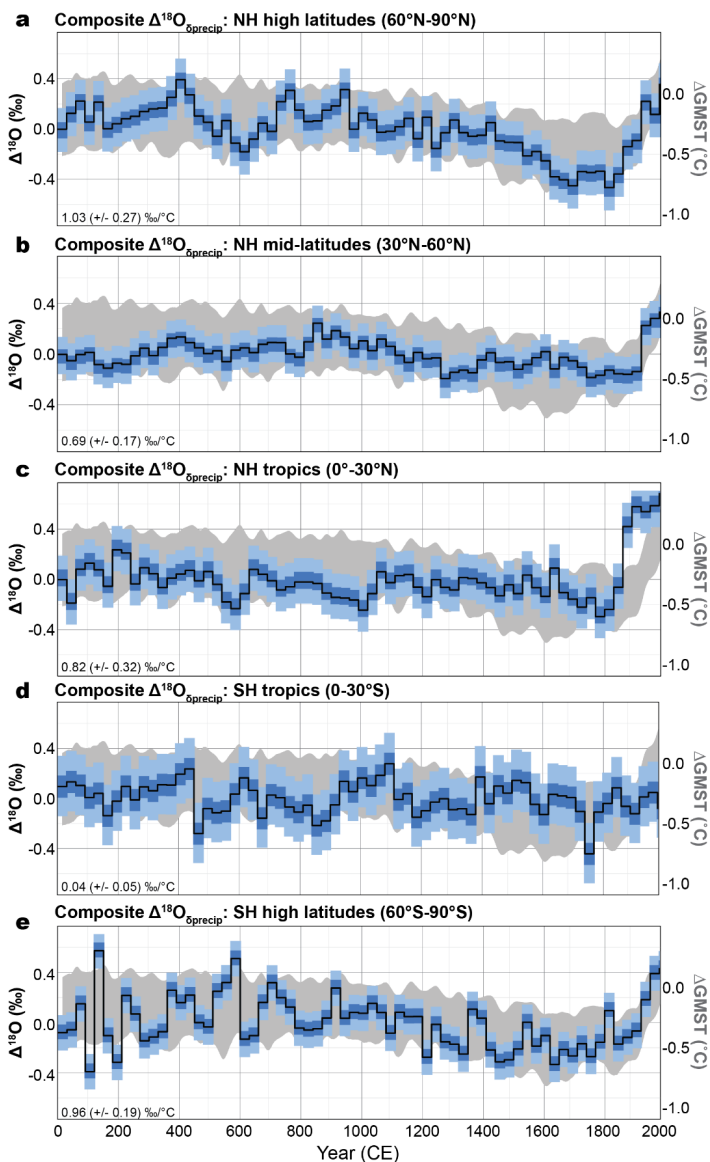
669 97.5 percentile of the 31-year Butterworth-filtered Global Mean Surface Temperature (GMST)

670 anomaly relative to the 1961-1990 mean¹.

671

672

673

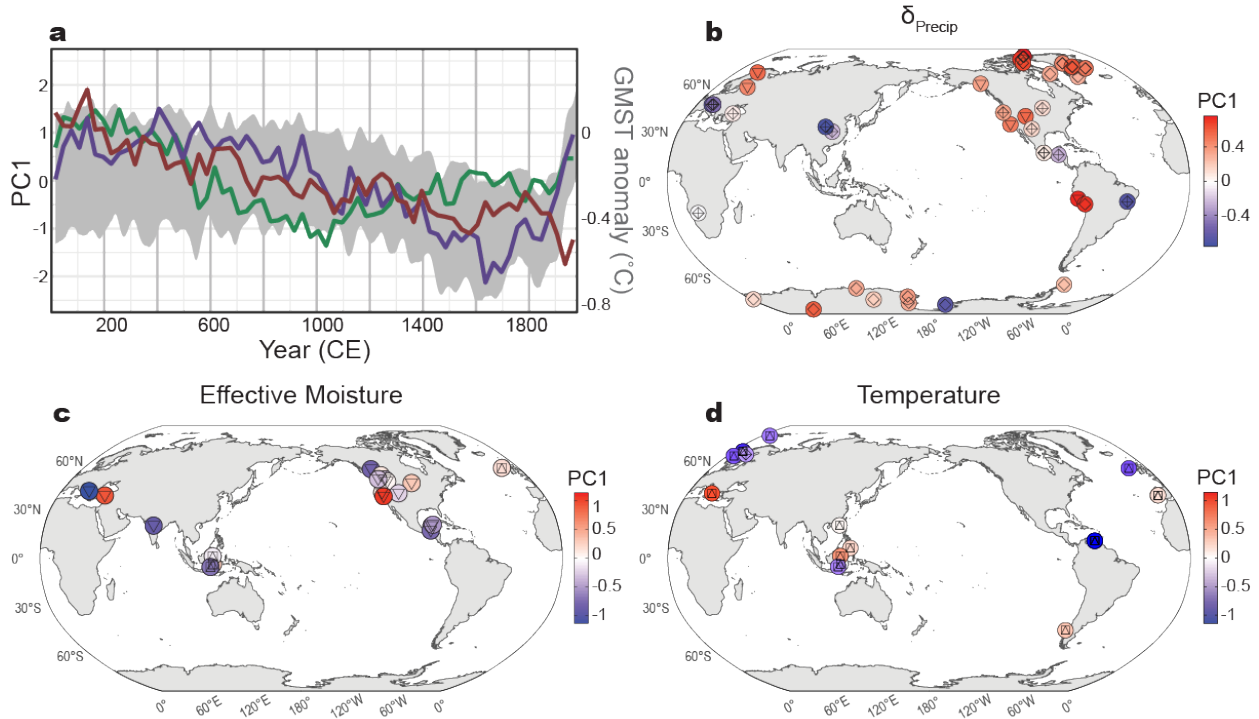


674

675 **Extended Data Figure 2. Composite $\Delta^{18}\text{O}_{\delta\text{precip}}$ calculated using Iso2k records¹⁵ falling**
 676 **within 30-degree latitudinal bins. a, 60-90°N (n=76); b, 30-60°N (n=86); c, 0-30°N (n=27); d,**
 677 **0-30°S (n=39); e, 60-90°S (n=77).** As per Fig. 1, black line with coloured shading shows the 30-
 678 year binned proxy $\delta^{18}\text{O}$ anomaly (black line, ensemble median; dark shading, first and third
 679 quantiles; light shading, 2.5th/97.5th percentiles) and gray shading depicts the ensemble 2.5 and
 680 97.5 percentile of the 31-year Butterworth-filtered GMST anomaly relative to the 1961-1990
 681 mean. Black text denotes mean regression slope (± 1 standard deviation) of regional composite

682 $\Delta^{18}\text{O}$ vs. GMST from 850-2000. Regional composite for 30-60°S not calculated due to
 683 insufficient number of records from those latitudes (n=2).

684

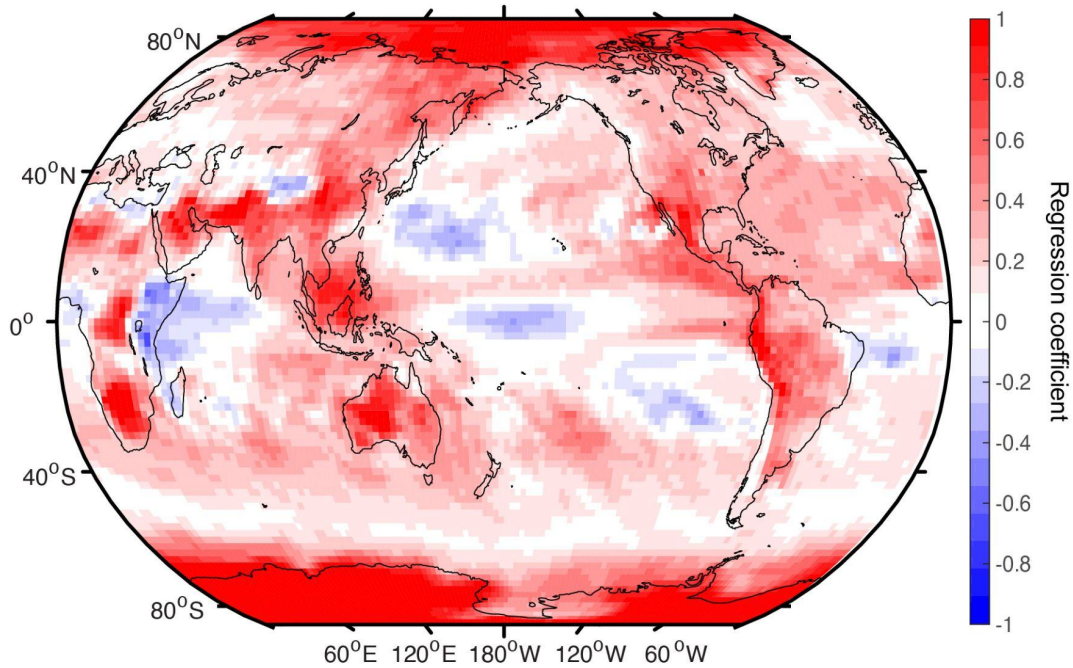


Archive (inner symbol): \diamond Ice \square Marine sediment \triangle Wood ∇ Lake sediment \diamond Speleothem
 — Precipitation $\delta^{18}\text{O}$ or $\delta^2\text{H}$ (δ_{Precip}) — Effective Moisture — Temperature

685

686 **Extended Data Figure 3. First Principal Component (PC1) of Iso2k records¹⁵ during the**
 687 **full Common Era.** Symbols, lines, and shading are as in Fig. 2 but for the interval 0-1980 (30-
 688 year bins), and without trends depicted (i.e. constant shape for outer symbols). δ_{precip} PC1
 689 explains 19% of the total variance (n = 44). Effective Moisture PC1 explains 19% of the total
 690 variance (n = 19). Temperature PC1 explains 25% of the total variance (n = 19). Maps created in
 691 R using coastlines from Natural Earth.

692



693

694 **Extended Data Figure 4. iCESM relationship between GMST and grid cell-level $\delta^{18}\text{O}_{\text{precip}}$.**

695 Shading depicts the regression coefficient in ‰/°C between mean annual, amount-weighted, 30-

696 year running mean $\delta^{18}\text{O}_{\text{precip}}$ at every grid cell vs. 30-year running mean, area-weighted GMST

697 for the mean of 3 full-forcing, isotope-enabled Last Millennium Ensemble members. Map

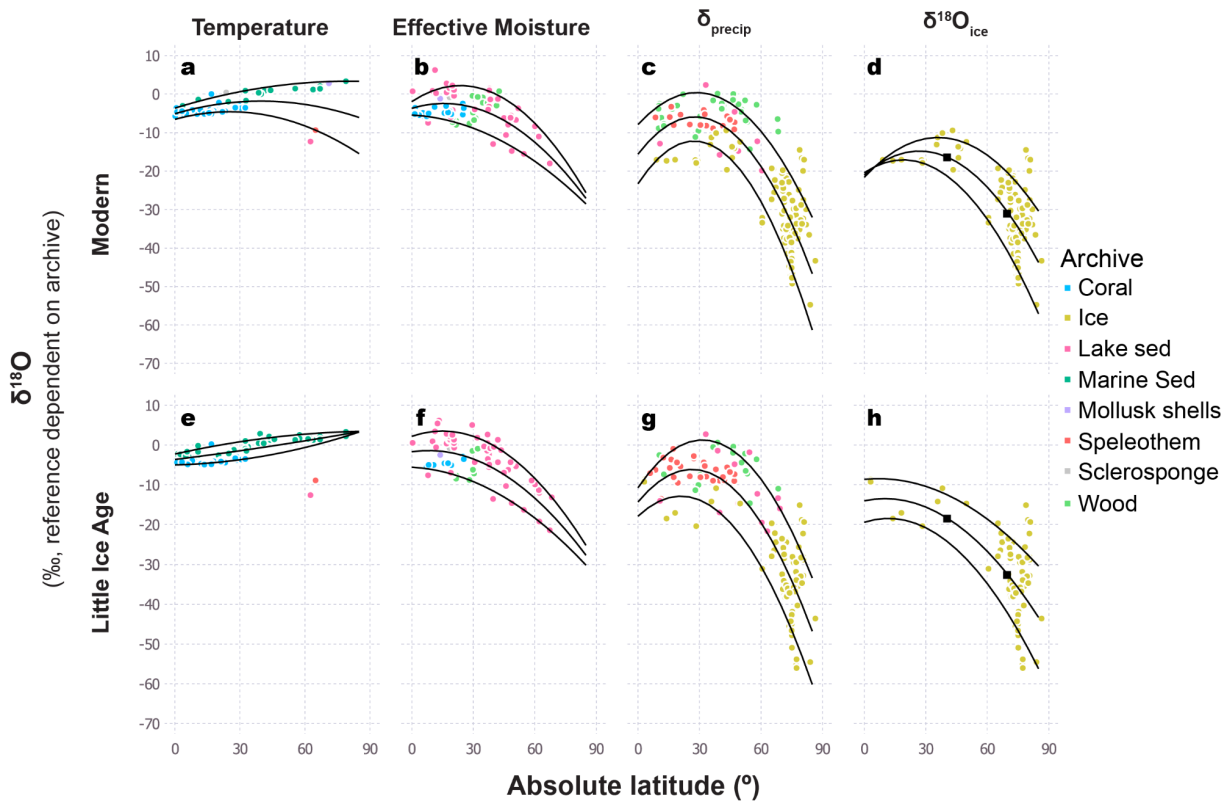
698 created in MATLAB using `m_map` for coastlines.

699

700

701

702



703

704 **Extended Data Figure 5. $\delta^{18}\text{O}$ vs. latitude in the Iso2k database¹⁵ for the modern era (a-d;**

705 **1950-2018) and the Little Ice Age (e-h; 1450-1850).** Data are plotted for the three main isotope

706 interpretation categories (a-c, e-g) and for $\delta^{18}\text{O}$ of glacier and ground ice (d, h), the archives that

707 preserve precipitation most directly. Black lines indicate polynomial fits to the 0.1, 0.5, and 0.9

708 quantiles. Black squares on panels (d) and (h) indicate 40 and 70 degrees latitude, the interval for

709 which the mean of the gradient function was calculated ($-0.48\text{‰}/^\circ$ latitude for both time periods;

710 see main text). All records are plotted in permil on the VSMOW-SLAP scale for ice core

711 records; PDB or VPDB for all other archives).

712

713

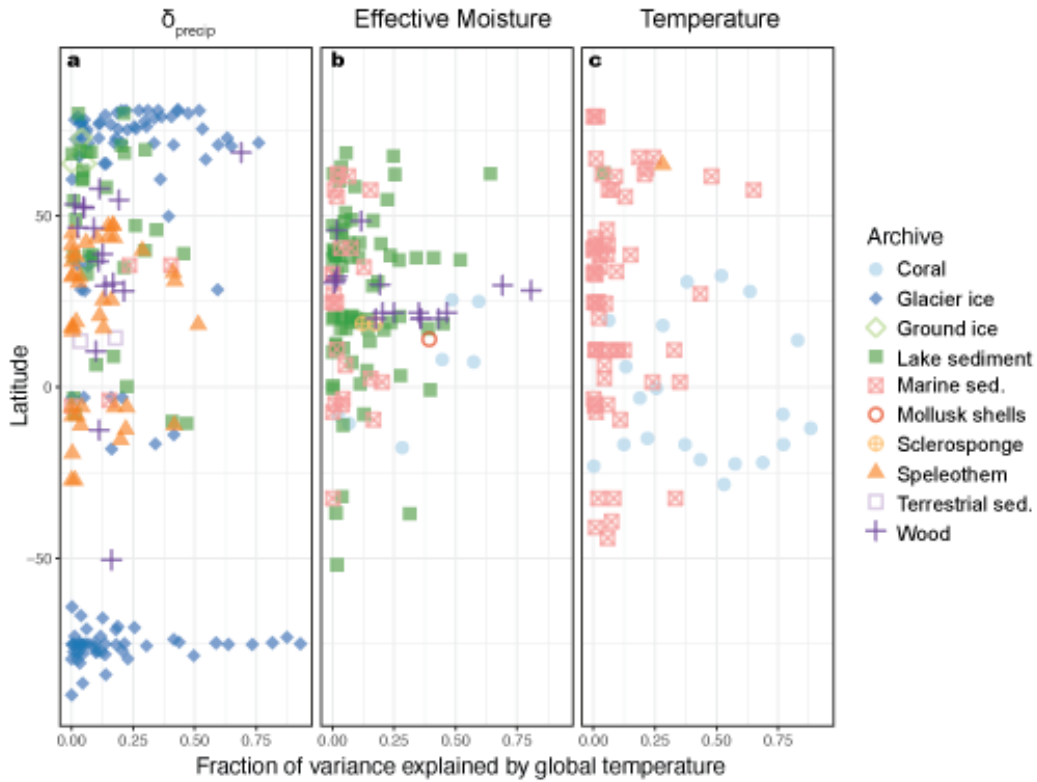
714

715

716

717

718



719

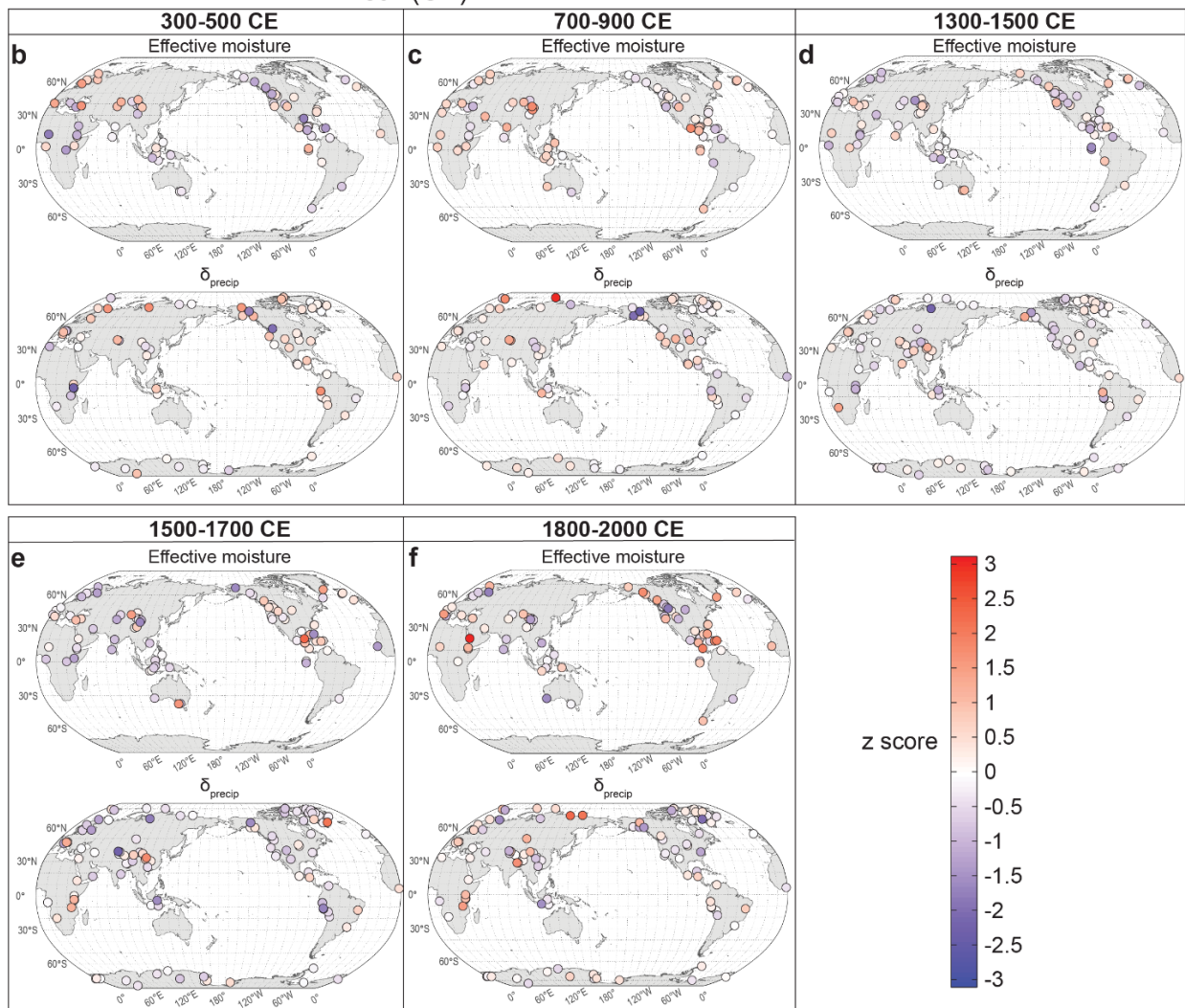
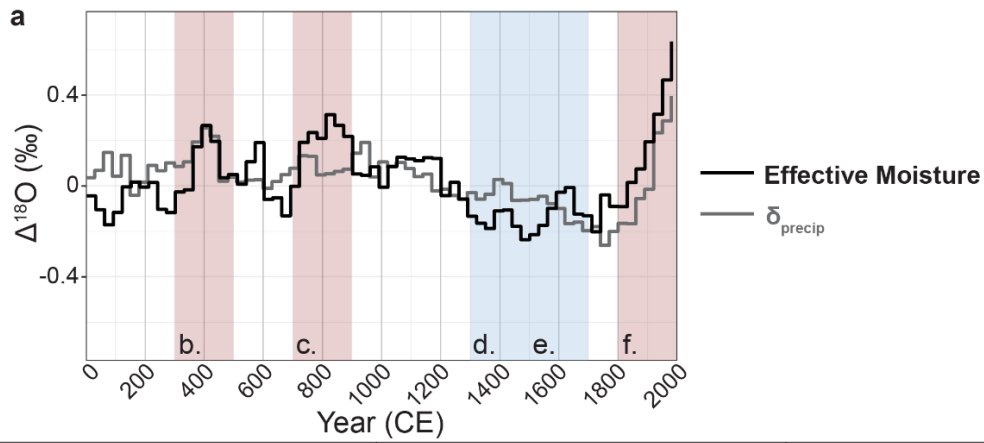
720 **Extended Data Figure 6. Relation between Iso2k¹⁵ primary timeseries and Global Mean**
 721 **Surface Temperature (GMST). (a) Fraction of variance explained (R^2) in δ_{precip} primary time**
 722 **series by changes in PAGES 2k global mean surface temperature (GMST) over the past 2000**
 723 **years. Both Iso2k time series and GMST were averaged into 30 year bins before calculating**
 724 **correlations (See Methods). (b) As in (a), but for Effective Moisture primary time series. (c) As**
 725 **in (a), but for Temperature primary time series.**

726

727

728

729



731 **Extended Data Figure 7. Standardized 200-year $\delta^{18}\text{O}$ anomalies from Effective Moisture**
732 **and δ_{precip} records. a,** Composite medians for Iso2k¹⁵ Effective Moisture and δ_{precip} driven
733 records, as shown in Fig. 1 of the main text. Red shading denotes intervals of relatively high
734 composite $\Delta^{18}\text{O}_{\text{EM}}$, and blue shading denotes intervals of relatively low composite $\Delta^{18}\text{O}_{\text{EM}}$. **b-f,**
735 Isotopic anomalies in individual EM and δ_{precip} records contributing to the composites during
736 those shaded intervals, via standardised anomaly maps for time intervals discussed in the main
737 text (see Methods). These maps only include records with data spanning ≥ 600 years.
738 Standardized anomalies at each site are relative to the Common Era mean value for that record.
739 Maps created in R using coastlines from Natural Earth.

740

741

742

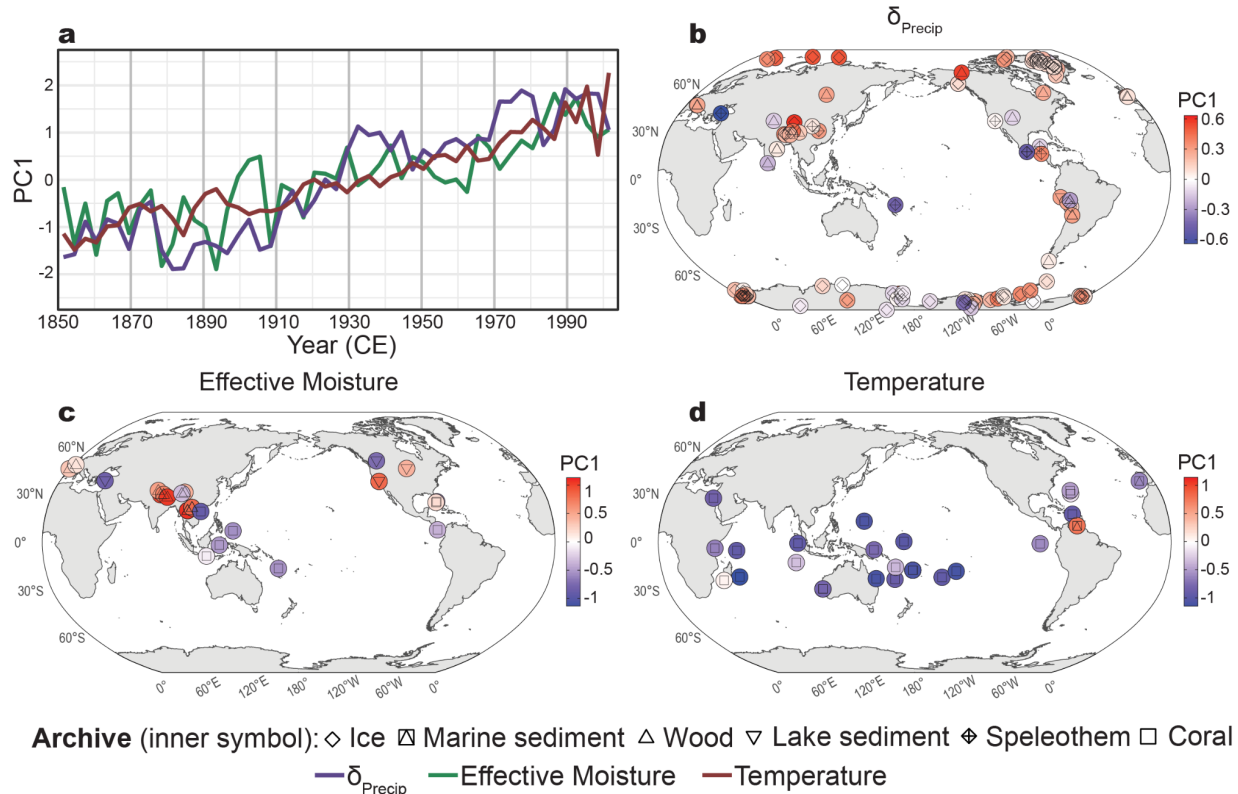
743

744

745

746

747



748

749

750 **Extended Data Figure 8. First Principal Component (PC1) of Iso2k data¹⁵ for the Historical**

751 **Period.** Symbols, lines, and shading are as per Extended Data Fig. 3, but for the interval 1850-

752 2005, with 3-year bins. δ_{precip} PC1 explains 12% of the total variance (n = 109). Effective

753 Moisture PC1 explains 32% of the total variance (n = 29). Temperature PC1 explains 38% of the

754 total variance (n = 27). Maps created in R using coastlines from Natural Earth.

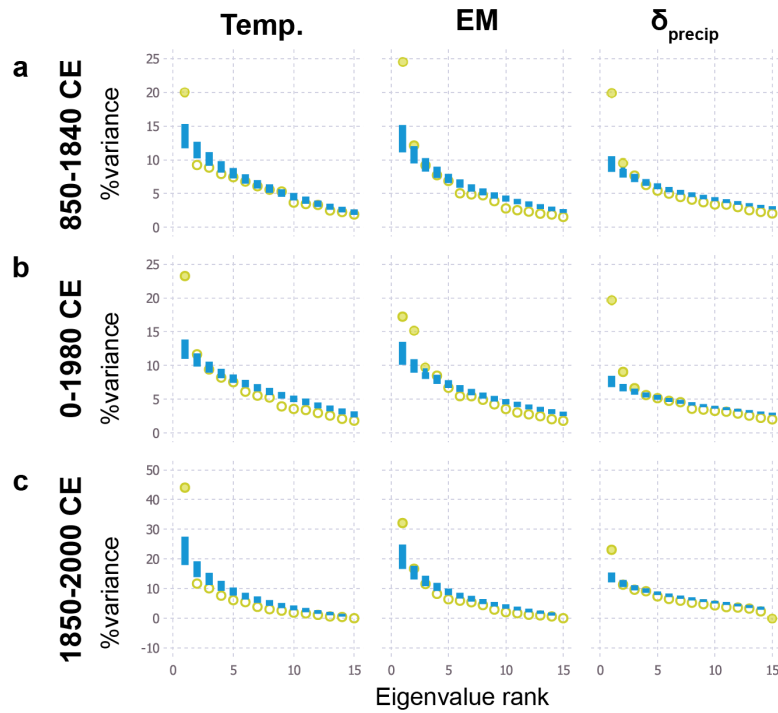
755

756

757

758

759



760

761 **Extended Data Figure 9. Significance of Iso2k¹⁵ PCA eigenvalues with respect to a null**

762 **hypothesis of stochastic forcing with decadal persistence. a,** Block bootstrap results from 850-

763 1840 with a 30-year bin width, 10-year block length, and tolerance of up to 15% missing data

764 (i.e., 85% coverage during the time interval; Methods). Yellow symbols depict the eigenvalues

765 (expressed as a percentage of the total variance) of each principal component. Blue bars show the

766 1-99% confidence intervals of the stochastic null hypothesis (n=1000). Eigenvalues above the

767 99% confidence interval are significant at the 1% level (one-sided test) and therefore are unlikely

768 to have arisen stochastically, and unlikely to be an artifact of the data processing steps (i.e.,

769 binning and interpolation). **(b)** as in **(a)** but for 0-1980. **(c)** as in **(a)** but for 1850-2000 and with a

770 10-year bin width and tolerance of up to 10% missing data (90% coverage).

771

772

773

774
775
776
777
778

REFERENCES

- 779 1. PAGES 2k Consortium. Consistent multidecadal variability in global temperature
780 reconstructions and simulations over the Common Era. *Nature Geoscience* **12**, 643–649
781 (2019).
- 782 2. PAGES 2k Consortium. A global multiproxy database for temperature reconstructions of the
783 Common Era. *Sci Data* **4**, 170088 (2017).
- 784 3. Field, C. B. *et al.* Part A: Global and sectoral aspects. Contribution of Working Group II to
785 the Fifth Assessment Report of the Intergovernmental Panel on Climate Change. in *Climate*
786 *Change 2014: Impacts, Adaptation, and Vulnerability* (Cambridge University Press, 2014).
- 787 4. Smerdon, J. E. *et al.* Comparing proxy and model estimates of hydroclimate variability and
788 change over the Common Era. *Proxy Use-Development-Validation/Terrestrial*
789 *Archives/Centennial-Decadal* (2017) doi:10.5194/cp-2017-37-RC1.
- 790 5. Dansgaard, W. Stable isotopes in precipitation. *Tellus* **16**, 436–468 (1964).
- 791 6. Rozanski, K. Isotopes in Atmospheric Moisture. in *Isotopes in the Water Cycle* (eds.
792 Aggarwal, P. K., Gat, J. R. & Froehlich, K. F.) 291–302 (Springer, 2005). doi:10.1007/1-
793 4020-3023-1_18.
- 794 7. Bowen, G. J., Cai, Z., Fiorella, R. P. & Putman, A. L. Isotopes in the Water Cycle:
795 Regional- to Global-Scale Patterns and Applications. *Annual Review of Earth and Planetary*
796 *Sciences* vol. 47 453–479 Preprint at <https://doi.org/10.1146/annurev-earth-053018-060220>
797 (2019).
- 798 8. Galewsky, J. *et al.* Stable isotopes in atmospheric water vapor and applications to the

- 799 hydrologic cycle. *Reviews of Geophysics* **54**, 809–865 (2016).
- 800 9. Konecky, B. L., Noone, D. C. & Cobb, K. M. The Influence of Competing Hydroclimate
801 Processes on Stable Isotope Ratios in Tropical Rainfall. *Geophys. Res. Lett.* **46**, 1622–1633
802 (2019).
- 803 10. Jasechko, S. Global isotope hydrogeology—review. *Rev. Geophys.* **57**, 835–965 (2019).
- 804 11. Sturm, C., Zhang, Q. & Noone, D. An introduction to stable water isotopes in climate
805 models: benefits of forward proxy modelling for paleoclimatology, *Clim. Past*, **6**, 115–129.
806 Preprint at (2010).
- 807 12. Gat, J. *Isotope Hydrology: A Study of the Water Cycle*. vol. 6 (Imperial College Press,
808 2010).
- 809 13. Craig, H. & Gordon, L. I. Deuterium and oxygen 18 variations in the ocean and the marine
810 atmosphere. in *Stable Isotopes in Oceanographic Studies and Paleotemperatures* (ed.
811 Tongiorgi, E.) 9–130 (Consiglio Nazionale Delle Ricerche, Laboratorio di Geologia
812 Nucleare - Pisa, 1965).
- 813 14. Rohling, E. J. PALEOCEANOGRAPHY, PHYSICAL AND CHEMICAL PROXIES |
814 Oxygen Isotope Composition of Seawater. in *Encyclopedia of Quaternary Science (Second*
815 *Edition)* (eds. Elias, S. A. & Mock, C. J.) 915–922 (Elsevier, 2013). doi:10.1016/B978-0-
816 444-53643-3.00293-4.
- 817 15. Konecky, B. L. *et al.* The Iso2k database: a global compilation of paleo- $\delta^{18}\text{O}$ and $\delta^2\text{H}$
818 records to aid understanding of Common Era climate. *Earth Syst. Sci. Data* **12**, 2261–2288
819 (2020).
- 820 16. Urey, H. C. Oxygen isotopes in nature and in the laboratory. *Science* **108**, 489–496 (1948).
- 821 17. Kaufman, D. *et al.* Holocene global mean surface temperature, a multi-method

- 822 reconstruction approach. *Sci Data* **7**, 201 (2020).
- 823 18. Brady, E. *et al.* The Connected Isotopic Water Cycle in the Community Earth System Model
824 Version 1. *Journal of Advances in Modeling Earth Systems* vol. 11 2547–2566 Preprint at
825 <https://doi.org/10.1029/2019ms001663> (2019).
- 826 19. Stevenson, S. *et al.* Volcanic Eruption Signatures in the Isotope-Enabled Last Millennium
827 Ensemble. *Paleoceanography and Paleoclimatology* **34**, 1534–1552 (2019).
- 828 20. Otto-Bliesner, B. L. *et al.* Climate Variability and Change since 850 CE: An Ensemble
829 Approach with the Community Earth System Model. *Bull. Am. Meteorol. Soc.* **97**, 735–754
830 (2016).
- 831 21. Thompson, D. M. *et al.* Identifying hydro-sensitive coral $\delta^{18}\text{O}$ records for improved high-
832 resolution temperature and salinity reconstructions. *Geophys. Res. Lett.* **49**, (2022).
- 833 22. Dansgaard, W. Stable isotopes in precipitation. *Tellus* **16**, 436–468 (1964).
- 834 23. Rozanski, K., Araguás-Araguás, L. & Gonfiantini, R. Isotopic patterns in modern global
835 precipitation. in *Climate Change in Continental Isotopic Records* (eds. Stewart, P. K.,
836 Lohmann, K. C., McKenzie, J. & Savin, S.) vol. 78 1–36 (American Geophysical Union,
837 1993).
- 838 24. Petit, J. R. *et al.* Climate and atmospheric history of the past 420,000 years from the Vostok
839 ice core, Antarctica. *Nature* **399**, 429–436 (1999).
- 840 25. Guan, J. *et al.* Understanding the temporal slope of the temperature-water isotope relation
841 during the deglaciation using isoCAM3: The slope equation. *J. Geophys. Res.* **121**, (2016).
- 842 26. Dansgaard, W. Stable isotopes in precipitation. *Tellus* **16**, 436–468 (1964).
- 843 27. Majoube, M. Fractionnement en oxygene 18 et en deuterium entre l'eau et sa vapeur.
844 *Journal de Chimie Physique* **68**, 1423–1436 (1971).

- 845 28. Craig, H., Gordon, L. I. & Horibe, Y. Isotopic exchange effects in the evaporation of water:
846 1. Low-temperature experimental results. *J. Geophys. Res. C: Oceans* **68**, 5079–5087
847 (1963).
- 848 29. Horita, J., Rozanski, K. & Cohen, S. Isotope effects in the evaporation of water: a status
849 report of the Craig-Gordon model. *Isotopes Environ. Health Stud.* **44**, 23–49 (2008).
- 850 30. Dansgaard, W. Stable isotopes in precipitation. *Tellus* **16**, 436–468 (1964).
- 851 31. Nusbaumer, J., Wong, T. E., Bardeen, C. & Noone, D. Evaluating hydrological processes in
852 the Community Atmosphere Model Version 5 (CAM5) using stable isotope ratios of water.
853 *J. Adv. Model. Earth Syst.* **9**, 949–977 (2017).
- 854 32. Aggarwal, P. K. *et al.* Stable isotopes in global precipitation: A unified interpretation based
855 on atmospheric moisture residence time. *Geophys. Res. Lett.* **39**, L11705 (2012).
- 856 33. Held, I. M. & Soden, B. J. Robust responses of the hydrological cycle to global warming. *J.*
857 *Clim.* **19**, 5686–5699 (2006).
- 858 34. Gat, J. R., Mook, W. G. & Meijer, H. A. *Environmental Isotopes in the Hydrological Cycle*,
859 *2nd ed.* vol. 2 (International Atomic Energy Agency, Vienna, Austria, 2001).
- 860 35. Siler, N. *et al.* The large-scale, long-term coupling of temperature, hydrology, and water
861 isotopes. *J. Clim.* 1–51 (2021) doi:10.1175/jcli-d-20-0563.1.
- 862 36. Bailey, A., Posmentier, E. & Feng, X. Patterns of evaporation and precipitation drive global
863 isotopic changes in atmospheric moisture. *Geophys. Res. Lett.* **45**, 7093–7101 (2018).
- 864 37. Neukom, R., Steiger, N., Gómez-Navarro, J. J., Wang, J. & Werner, J. P. No evidence for
865 globally coherent warm and cold periods over the preindustrial Common Era. *Nature* **571**,
866 550–554 (2019).
- 867 38. Falster, G., Konecky, B., Madhavan, M., Stevenson, S. & Coats, S. Imprint of the Pacific

- 868 Walker Circulation in Global Precipitation $\delta^{18}\text{O}$. *J. Clim.* **34**, 8579–8597 (2021).
- 869 39. Putman, A. L., Bowen, G. J. & Strong, C. Local and regional modes of hydroclimatic
870 change expressed in modern multidecadal precipitation oxygen isotope trends. *Geophys.*
871 *Res. Lett.* **48**, (2021).
- 872 40. Stuiver, M., Grootes, P. M. & Braziunas, T. F. The GISP2 $\delta^{18}\text{O}$ Climate Record of the Past
873 16,500 Years and the Role of the Sun, Ocean, and Volcanoes. *Quat. Res.* **44**, 341–354
874 (1995).
- 875 41. Vuille, M. *et al.* A review of the South American Monsoon history as recorded in stable
876 isotopic proxies over the past two millennia. *Clim. Past* **8**, 1309–1321 (2012).
- 877 42. Zhao, K. *et al.* A high-resolved record of the Asian Summer Monsoon from Dongge Cave,
878 China for the past 1200 years. *Quat. Sci. Rev.* **122**, 250–257 (2015).
- 879 43. Konecky, B. L. *et al.* Intensification of southwestern Indonesian rainfall over the past
880 millennium. *Geophys. Res. Lett.* **40**, 386–391 (2013).
- 881 44. Cook, E. R., Seager, R., Cane, M. A. & Stahle, D. W. North American drought:
882 Reconstructions, causes, and consequences. *Earth-Sci. Rev.* **81**, 93–134 (2007).
- 883 45. Shuman, B. N. *et al.* Placing the Common Era in a Holocene context: millennial to
884 centennial patterns and trends in the hydroclimate of North America over the past 2000
885 years. *Clim. Past* **14**, 665–686 (2018).
- 886 46. Li, J., Xie, S.-P. & Cook, E. R. El Niño phases embedded in Asian and North American
887 drought reconstructions. *Quat. Sci. Rev.* **85**, 20–34 (2014).
- 888 47. Bjerknes, J. Atmospheric teleconnections from the equatorial Pacific. *Mon. Weather Rev.*
889 **97**, 163–172 (1969).
- 890 48. Kong, W. & Chiang, J. C. H. Southward shift of westerlies intensifies the east Asian early

- 891 summer rainband following El Niño. *Geophys. Res. Lett.* **47**, (2020).
- 892 49. Seager, R. *et al.* Adjustment of the atmospheric circulation to tropical Pacific SST
893 anomalies: Variability of transient eddy propagation in the Pacific-North America sector.
894 *Quart. J. Roy. Meteor. Soc.* **136**, 277–296 (2010).
- 895 50. Wittenberg, A. T. Are historical records sufficient to constrain ENSO simulations? *Geophys.*
896 *Res. Lett.* **36**, L12702 (2009).
- 897 51. Collins, M. *et al.* The impact of global warming on the tropical Pacific Ocean and El Niño.
898 *Nat. Geosci.* **3**, 391–397 (2010).
- 899 52. Vecchi, G. *et al.* Weakening of tropical Pacific atmospheric circulation due to anthropogenic
900 forcing. *Nature* **441**, 73–76 (2006).
- 901 53. Konecky, B. L. & McKay, N. P. NOAA/WDS Paleoclimatology - The Iso2k Database.
902 NOAA National Centers for Environmental Information. (2020) doi:10.25921/57j8-vs18.
- 903 54. Craig, H. Isotopic Variations in Meteoric Waters. *Science* **133**, 1702–1703 (1961).
- 904 55. Beckers, J.-M., Barth, A. & Alvera-Azcárate, A. DINEOF reconstruction of clouded images
905 including error maps—application to the Sea-Surface Temperature around Corsican Island.
906 *Ocean Science* **2**, 183–199 (2006).
- 907 56. Alvera-Azcárate, A., Barth, A., Sirjacobs, D., Lenartz, F. & Beckers, J.-M. Data
908 Interpolating Empirical Orthogonal Functions (DINEOF): a tool for geophysical data
909 analyses. *Mediterr. Mar. Sci.* **12**, 5–11 (2011).
- 910 57. Oksanen, J., Kindt, R., Legendre, P. & Others. Vegan: community ecology package. R
911 package version 2.2-1. R Development Core Team, Vienna. Preprint at (2015).
- 912 58. Wong, T. E., Nusbaumer, J. & Noone, D. C. Evaluation of modeled land-atmosphere
913 exchanges with a comprehensive water isotope fractionation scheme in version 4 of the

- 914 Community Land Model. *J. Adv. Model. Earth Syst.* **9**, 978–1001 (2017).
- 915 59. Allan, R. & Ansell, T. A New Globally Complete Monthly Historical Gridded Mean Sea
916 Level Pressure Dataset (HadSLP2): 1850–2004. *J. Clim.* **19**, 5816–5842 (2006).